

Article

Study on Friction and Corrosion Performance of CrTiBN Coating in Artificial Seawater Environment

Man Li ^{1,*}, Yunjiang Yu ², Changwei Zou ³, Canxin Tian ³ and Yanxiong Xiang ³¹ Faculty of Mechanical and Electrical Engineering, Lingnan Normal University, Zhanjiang 524048, China² Faculty of Chemistry and Chemical Engineering, Lingnan Normal University, Zhanjiang 524048, China³ Faculty of Physics Science and Technology, Lingnan Normal University, Zhanjiang 524048, China

* Correspondence: oqlm@163.com

Abstract: CrN, CrTiN, and CrTiBN coatings were deposited onto 316 stainless steel substrates using multi-arc ion plating techniques. Their morphology, microstructures, friction performance, and corrosion resistance in simulated seawater were systematically characterized. After being analyzed with X-ray diffraction, X-ray photoelectron spectroscopy, and scanning electron microscopy, the results revealed that CrN coatings had a primary face-centered cubic CrN structure. Following the addition of Ti and B elements, CrTiBN coatings exhibited a cross-sectional structure with hexagonal TiB₂ and amorphous BN, displaying the most compact structure. Electrochemical impedance spectroscopy tests indicated that CrTiBN coatings had the highest polarization resistance, the highest phase angle, and the widest frequency range. During electrochemical polarization curve tests, CrTiBN coatings displayed a corrosion potential of 0.11 V, a polarization resistance of 2470 kΩ·cm², and a minimal corrosion current of 1.94×10^{-8} A/cm², demonstrating outstanding corrosion resistance. The results from the friction tests indicated that CrTiBN coatings exhibited the lowest friction coefficients of 0.16 and wear rates of 8.18×10^{-7} mm³/Nm. Insights gained from electrochemical friction–corrosion tests revealed that CrTiBN coatings maintained the highest Open Circuit Potential (OCP) throughout the corrosion and friction process. In summary, the introduction of Ti and B has clearly enhanced the friction and corrosion resistance properties of CrTiBN coatings in comparison to CrN coatings.



Citation: Li, M.; Yu, Y.; Zou, C.; Tian, C.; Xiang, Y. Study on Friction and Corrosion Performance of CrTiBN Coating in Artificial Seawater Environment. *Coatings* **2023**, *13*, 1837. <https://doi.org/10.3390/coatings13111837>

Academic Editor: Edoardo Proverbio

Received: 19 September 2023

Revised: 12 October 2023

Accepted: 23 October 2023

Published: 27 October 2023



Copyright: © 2023 by the authors. Licensee MDPI, Basel, Switzerland. This article is an open access article distributed under the terms and conditions of the Creative Commons Attribution (CC BY) license (<https://creativecommons.org/licenses/by/4.0/>).

Keywords: CrTiBN coatings; corrosion resistance; wear mechanism; artificial seawater

1. Introduction

In the midst of the rapid expansion of the maritime economy, the necessity to enhance the corrosion resistance and wear resilience of marine engineering equipment in seawater environments is progressively escalating [1–3]. Marine engineering equipment operates within marine environments for extended durations, enduring the dual impacts of friction and corrosion, resulting in equipment malfunction and profoundly jeopardizing its longevity and safety [4]. Among the materials used for marine engineering equipment, 316 stainless steel plays a pivotal role due to its cost-effectiveness, satisfactory mechanical properties, and corrosion resistance, making it widely adopted. Nonetheless, studies indicate that 316 stainless steel is prone to substantial degradation and failure in high-chloride corrosive solutions due to the alternating interplay between electrochemical corrosion and mechanical wear [5–7]. In order to augment the anti-wear and corrosion-resistant properties of equipment materials without altering the substrate's fundamental characteristics, the application of protective coatings on material surfaces through diverse deposition techniques is a viable approach. Thanks to their outstanding attributes in terms of oxidation resistance, wear resistance, and corrosion resistance, CrN coatings have been extensively employed for the protection of surfaces on maritime equipment [7,8]. Nonetheless, CrN coatings are characterized by a microstructure featuring coarse-grained columnar crystals, rendering them susceptible to the intrusion of chloride ions from seawater through intergranular gaps,

thereby instigating substrate corrosion [9]. A comprehensive study of the friction–corrosion behavior and mechanisms of these coatings in marine corrosive environments will offer both experimental and theoretical support for the utilization of engineering equipment under challenging marine conditions.

In the quest of creating enduring protective coatings, researchers have dedicated efforts to fabricating ternary or multi-component CrN coatings [10]. In practical investigations, a common approach involves incorporating metallic elements (such as Ti, Al, V) [11–14] or non-metallic elements (such as Si, C, B) [15–20] into conventional binary CrN coatings, thus forming ternary or multi-component alloyed coatings that elevate resistance against corrosion and wear [11–20].

The incorporation of Ti into CrN coatings effectively enhances their wear and corrosion resistance, making them extensively utilized in the field of coating protection. Zhang et al. [10] utilized medium-frequency magnetron sputtering to fabricate CrTiN coatings and observed exceptional tribological performance of the coating during steel ball sliding in ambient air. Moreover, Kong et al. [21] utilized unbalanced magnetron sputtering to deposit CrTiN layers and discovered that replacing chromium atoms with titanium atoms led to the creation of a solid solution, $\text{Cr}_{1-x}\text{Ti}_x\text{N}$, exhibiting superior corrosion resistance compared to traditional CrN coatings. Despite the performance enhancement CrTiN coatings offer to CrN coatings, the existence of columnar crystal structure defects could potentially undermine their protective performance.

The addition of B elements to CrTiN coatings holds promise for mitigating inherent flaws within the coatings, such as pinholes, droplets, and microcracks. This improvement significantly highlights the potential benefits of enhanced corrosion resistance and wear resistance [22,23]. Lu et al. [24] produced CrTiBN coatings by combining high-power pulsed and medium-frequency magnetron sputtering. Their investigation revealed that these coatings exhibited a dense microstructure and an exceptionally smooth surface. The coefficients of friction and wear rates were remarkably low, measuring 0.46 and $2.06 \times 10^{-6} \text{ mm}^3/\text{Nm}$, respectively, showcasing exceptional adhesion and wear resistance. In contrast, Wang et al. [25] utilized magnetron sputtering techniques to create CrTiBN coatings, successfully elevating the mechanical properties and resistance to high compressive stress of CrN coatings. Yu et al. [26] produced CrTiBN coatings using a magnetron sputtering technique, concurrently adjusting the concentrations of Ti and B within the coatings. The results indicated that Cr-Ti-B-N coatings attained peak hardness and elastic modulus values of 28 and 283.6 GPa, respectively. Moreover, the addition of Ti and B elements significantly improved the friction and wear performance of the coatings when compared to CrN coatings.

Although CrTiBN coatings have garnered some interest regarding magnetron sputtering deposition and wear resistance, their corrosion behavior and tribocorrosion mechanisms in artificial seawater solutions remain not entirely elucidated. To tackle this situation, the current research employs the arc ion plating technique to deposit CrN, CrTiN, and CrTiBN coatings. The current research comprehensively investigates their microstructure, wear resistance, and corrosion resistance. Furthermore, a comprehensive analysis of the failure mechanisms of the coatings is undertaken. This research has the potential to offer a new experimental and theoretical foundation to better comprehend the behavior of CrTiBN coatings in marine settings.

2. Experimental Details

2.1. Coating Deposition

CrN, CrTiN, and CrTiBN coatings were synthesized on the surfaces of 316 stainless steel and single-crystal silicon utilizing multi-arc ion plating (AS510DTXB, Beijing Damp Surface Technology Co., Ltd., Beijing, China). Cathode targets of 99.9% purity TiB₂ alloy, 99.9% pure Cr, and 99.9% pure Ti were employed. The target bodies had dimensions of $\varnothing 100 \times 20 \text{ mm}$ each, maintaining a minimum center-to-center distance of 200 mm between the target and the substrate. The configuration of the deposition system is depicted in

Figure 1. Prior to the coating deposition process, the single-side polished 316 stainless steel and single-crystal silicon underwent a 20 min ultrasonic cleaning in acetone and anhydrous ethanol, respectively. Ar gas (99.99 at.%) served as the working gas, while N₂ gas (99.99 at.%) was used as the reactive gas. The chamber vacuum was evacuated to 3.0×10^{-3} Pa, and the chamber temperature was raised to 350 °C at a rate of 5 °C/min and maintained for 30 min. The primary deposition process is outlined as follows: (1) Etching is conducted in an argon atmosphere to raise the chamber vacuum to 8.0×10^{-2} Pa. The pulsed bias voltage is set to −800 V, and the substrate is etched for 15 min to eliminate surface oxides and other adherents. (2) Deposition of the transition layer CrN/Cr occurs, under a nitrogen atmosphere, the Cr target current is adjusted to 80 A, and the working pressure is maintained at 2.0 Pa for a deposition duration of 10 min. (3) Deposition of the CrTiBN layer occurs, under a nitrogen atmosphere, the Cr target current is adjusted to 80 A, and the TiB₂ target current is set to 70 A. The working pressure is maintained at 0.7 Pa, and the deposition continues for 90 min.

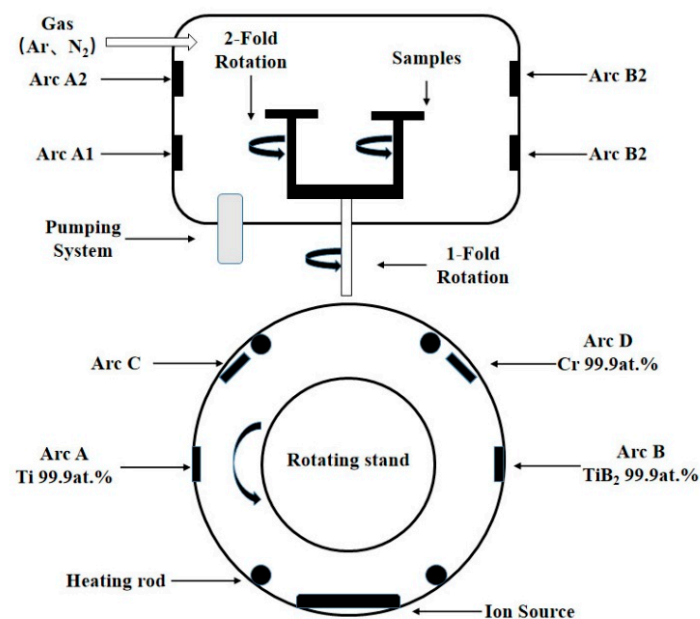


Figure 1. Schematic diagram of arc deposited coatings.

The deposition parameters for each coating are provided in Table 1.

Table 1. Deposition parameters of coatings.

Coatings	Temperature/°C	Current/A	Pressure/Pa	Current/A	Pressure/Pa	Time/min
CrN	350	80	2.0	80	1.0	90
CrTiN	350	80	2.0	80	1.0	90
CrTiBN	350	80	2.0	70	0.7	90

2.2. Characterization

The crystallographic structure of the coatings was examined through X-ray diffraction (XRD) utilizing a Bruker D8 advanced X-ray diffractometer (Bruker, Karlsruhe, Germany; Fällanden, Switzerland); X-ray photoelectron spectroscopy (XPS) was employed with an ESCALAB 250Xi instrument (Thermo Fisher, Waltham, MA, USA) to examine the chemical composition of the coatings; a Field Emission Scanning Electron Microscope (FE-SEM) model JSM-7610F (JEOL, Tokyo, Japan) was employed to observe the surface, wear traces, friction pair wear traces, and cross-sectional morphology of the coatings. The chemical composition analysis was conducted using an energy dispersive spectrometer (EDS) system, specifically NORAN System 7 (Thermo Fisher Inc., Waltham, MA, USA); the CMT-1

friction and wear testing machine (CMT-1, Huahui Instrument Company, Lanzhou, China) was utilized to measure the coefficient of friction of the coatings. Moreover, an optical profilometer (Bruker Contour GT K 3D, Billerica, Middlesex, MA, USA) was employed to examine the wear trace morphology of the coatings. The friction material utilized was a 4-mm-diameter SiC ball, which led to an 8 mm wear track diameter. The rotation speed was held at a constant 5 m/min, and the friction process continued for a duration of 100 min. The wear rate of the coating's wear track was determined using Equation (1), and the wear rate of the abrasive ball was calculated using Equation (2) [27]:

$$\omega_{s,b} = \frac{2\pi r A}{FL} \quad (1)$$

$$\omega_{s,a} = \frac{\pi d^4}{64RFL} \quad (2)$$

In the equation, d represents the diameter of the abrasive wear track (mm); R stands for the radius of the abrasive ball (mm); F denotes the applied load during the test (N); L signifies the length of the sliding distance (m); r corresponds to the radius of the coating wear trace (mm); and A represents the average worn area of the coating wear trace (mm²).

The electrochemical behavior of the coatings in artificial seawater was examined using an electrochemical workstation (PGSTAT100N, AutoLab, Karlsruhe, Germany). The artificial seawater composition adhered to the ASTM D1141-98 standard [28], with detailed parameters available in Table 2. The electrochemical impedance spectroscopy (EIS) was conducted under the open-circuit potential (OCP) mode with a sinusoidal perturbation of 10 mV and a frequency range from 10 mHz to 100 kHz. The potentiodynamic polarization curve was scanned in the range of -1.0 to 1.0 V at a scan rate of 20 mV/min. The corrosion–friction behavior of the coatings in an artificial seawater solution was investigated by employing an electrochemical corrosion–friction testing machine (MFT-EC400, Huahui Instrument Company, Lanzhou, China). During the reciprocating sliding process, a 5-mm-diameter silicon carbide ball was utilized with a load of 10 N, a stroke length of 4 mm, and a frequency of 0.1 Hz. i_{corr} and E_{corr} were obtained through Tafel extrapolation, while polarization resistance was calculated using the Stern–Geary equation, Equation (3) [29]:

$$i_{corr} = \frac{\beta_a \beta_c}{2.303 R_p (\beta_a + \beta_c)} \quad (3)$$

where β_a is the Tafel anodic polarization slope, and β_c is the Tafel cathodic polarization slope.

Table 2. Chemical composition of artificial seawater.

Component	NaCl	KCl	Na ₂ SO ₄	NaHCO ₃	MgCl ₂	KBr	CaCl ₂	H ₃ BO ₃	SrCl ₂	NaF
Concentration (g/L)	24.530	0.695	4.090	0.201	5.200	0.101	1.160	0.027	0.025	0.003

3. Results and Discussion

3.1. Morphology and Structure of the Coatings

Figure 2 depicts surface SEM images and EDS analyses of CrN, CrTiN, and CrTiBN coatings. The surfaces of all three coatings exhibit small droplets, pinholes, and melting craters with dimensions spanning from hundreds of nanometers to a few micrometers. These are typical surface imperfections encountered during the arc ion plating preparation process [30]. Among the three coatings, the CrN coating exhibits the smallest particle size on its surface, while the CrTiN coating has the largest particle size and shows a notable increase in surface defects. Compared to the CrTiN coating, the larger particles on the surface of the CrTiBN coating doped with B elements are considerably smaller. The melting craters are shallower, surface morphology is refined, and there is a significant improvement in the surface quality of the coating. This improvement is credited to the formation of

amorphous or nanocrystalline borides on the surface of the CrTiBN coating, which enhances the coating's density [31].

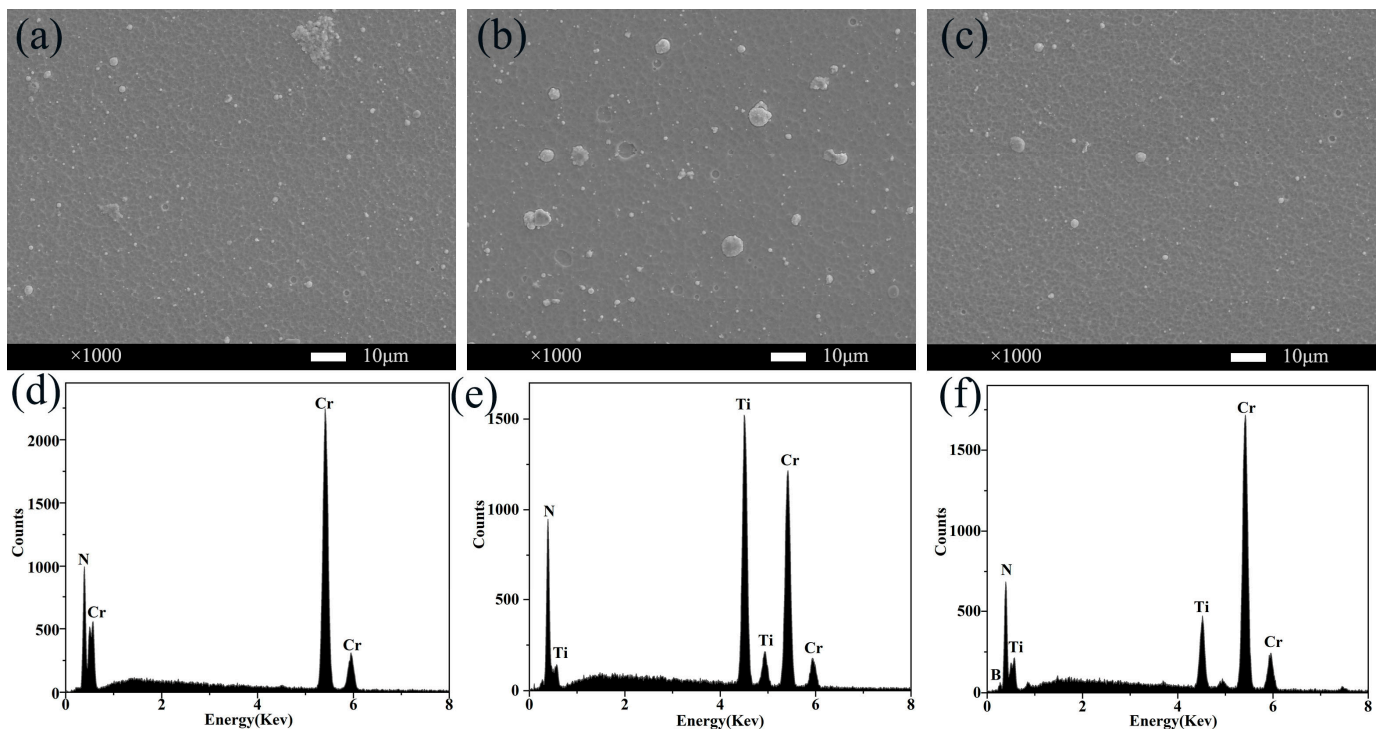


Figure 2. Surface morphological (a–c) and EDS spectra (d–f) images of CrN, CrTiN, and CrTiBN coatings.

Figure 3 depicts cross-sectional SEM images of the CrN, CrTiN, and CrTiBN coatings. The grain sizes for these coatings are provided in Table 3. In the case of the CrTiN coating, the average grain size measures at 5.64 nm, whereas the CrTiBN coating features the smallest grain size, measuring at 5.32 nm. The average grain size for the CrN coating is 6.48 nm. The coating thicknesses are approximately 2.471 μm, 3.439 μm, and 2.599 μm. It is worth noting that the cross-sectional view of the CrN coating reveals a distinct porous columnar crystal structure. The introduction of Ti elements through doping leads to the replacement of Cr atoms with more reactive Ti atoms, forming new TiN crystallites [21]. This process is elucidated in reference. As a consequence, the grain size decreases from 6.48 nm to 5.64 nm, leading to a denser structure in comparison to the CrN coating, while the columnar crystal arrangement remains unchanged. Upon incorporating B elements, the cross-sectional grain structure undergoes a transition from a columnar form to an irregular and densely packed microstructure. This results in a reduction in the grain size to 5.32 nm, consequently enhancing the coating's density. This transformation is attributed to the capability of the CrTiBN coating to form an amorphous or nanocrystalline BN structure. Within the CrN and TiN crystals, these structures exist as solid solutions, inducing lattice distortion and inhibiting the growth of columnar grains, ultimately refining the grain structure. This notable refinement substantially enhances the density of the CrTiN coating, as documented in references [18,26].

Table 3. Mechanical properties of CrN, CrTiN, and CrTiBN coatings.

Coatings	Hardness (HV)	Average Crystal Size (nm)
CrN	1965	6.48
CrTiN	2456	5.64
CrTiBN	2374	5.32

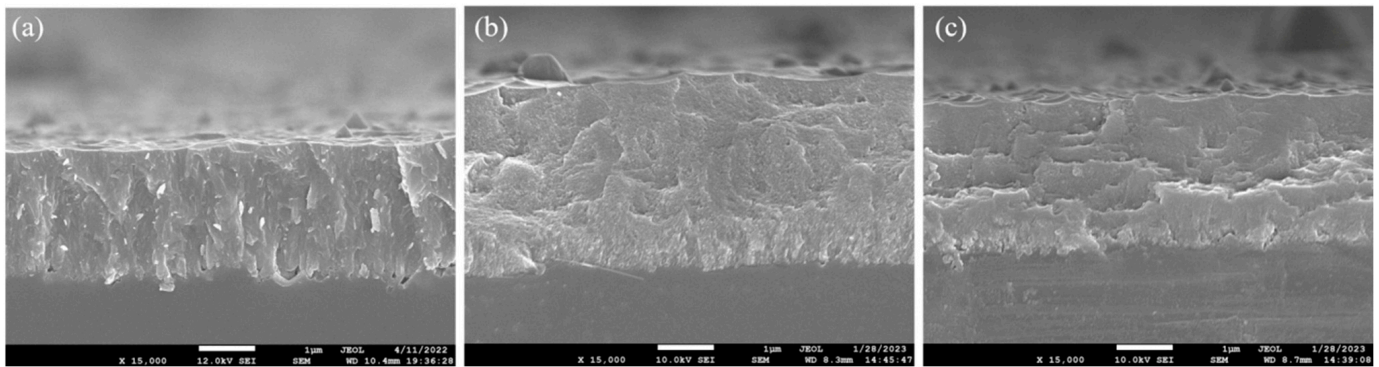


Figure 3. Cross-sectional (a–c) SEM images of CrN, CrTiN, and CrTiBN coatings.

Figure 4 displays the XRD patterns of the CrN, CrTiN, and CrTiBN coatings. The XRD spectrum of the CrN coating exhibits diffraction peaks assigned to CrN (111), CrN (200), CrN (220), and CrN (222), with a notable preference for the (200) plane. In the XRD spectrum of the CrTiN coating, the intensities of the CrN (111), CrN (200), and CrN (220) peaks decrease, and the CrN (222) peak nearly disappears. Due to the higher reactivity of Ti atoms compared to Cr atoms, the presence of the TiN (220) diffraction peak in the CrTiN coating is explained with the replacement of Cr atoms with Ti atoms, resulting in the formation of new TiN crystallites. With the introduction of B elements into the CrTiN coating, the peak widths of the CrN (111), CrN (200), CrN (220), and TiN (220) orientations increase. This could be attributed to the formation of amorphous BN structures due to the solid solution effect, causing lattice distortion and grain refinement [26]. Additionally, a new peak corresponding to TiB_2 (002) emerges in the CrTiBN coating. By applying the Scherrer equation, Equation (4), we can calculate the grain size of each coating, and the corresponding data are provided in Table 3:

$$D = \frac{k\lambda}{B\cos\theta} \quad (4)$$

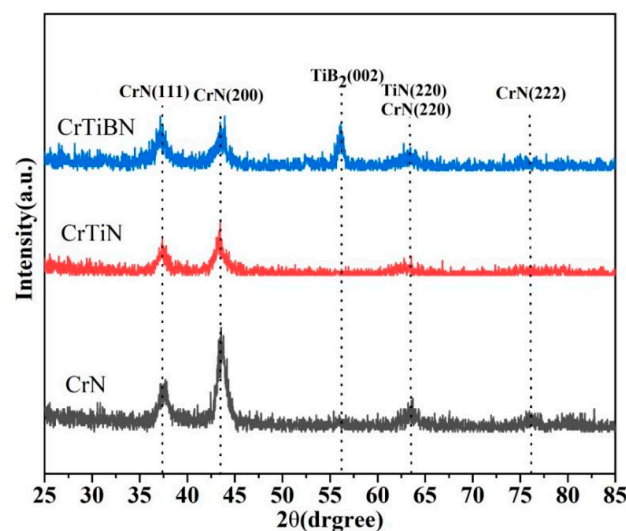


Figure 4. XRD patterns of CrN, CrTiN, and CrTiBN coatings.

Within this equation, D signifies the average grain size perpendicular to the hkl lattice planes, k is used to represent the Scherrer constant (set at 0.89), B represents the full width at half maximum (FWHM) of the diffraction peak, θ denotes the diffraction angle, and λ is the X-ray wavelength, specifically 0.15404 nm.

Figure 5 exhibits the B 1s and N 1s XPS core-level spectra of CrTiBN, which elucidate the chemical binding states of the elements within the coatings. Specifically, in the B 1s' spectrum fitting, a binding energy of 190.6 eV is indicative of B-N bonding, while 192.5 eV signifies B-O [32]. Furthermore, the N 1s' spectrum reveals four distinct peaks at binding energies of 396.1, 397.2, 398.8, and 399.8 eV, which correspond to the TiN [33], CrN [34], BN [35], and TiN [36] BN [35] phases, respectively. Moreover, research by Tian et al. suggests that the inclusion of B elements can promote the formation of an amorphous BN structure, which aids in grain refinement [32–37]. The results obtained from the XRD analysis (Figure 4) are corroborated with the XPS analysis (Figure 5), emphasizing the predominant presence of B atoms in the amorphous BN phase of the CrTiBN coating.

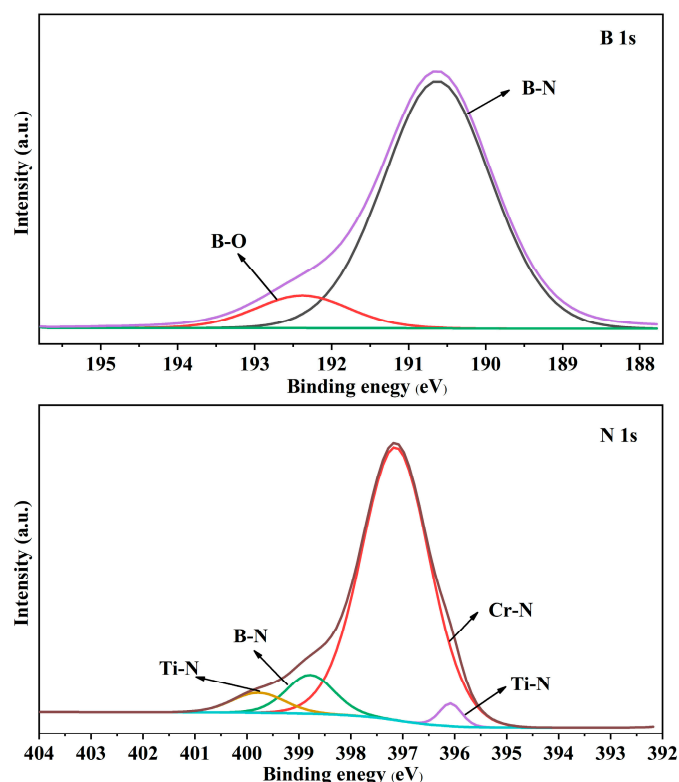


Figure 5. XPS spectra of CrTiBN coatings.

Table 3 showcases the hardness measurements for the CrN, CrTiN, and CrTiBN coatings. The CrN coating registers a hardness of 1965 HV, while the CrTiN and CrTiBN coatings display hardness values of 2456 HV and 2374 HV, respectively. The proximity of these values signifies their comparable hardness. With the introduction of Ti elements in the CrTiN coating, it assumes the form of TiN grains. The higher binding energy in Ti-N bonds, in contrast to Cr-N bonds, results in enhanced hardness for the CrTiN coating [38]. Comparatively, the CrTiBN coating possesses a denser structure and smaller grain size than the CrTiN coating. This grain refinement significantly contributes to the enhancement of the coating's hardness. However, it is essential to note that XPS data indicates the presence of B elements originating from the soft BN phase in the CrTiBN coating. This observation clarifies the similarity in hardness between the CrTiBN and CrTiN coatings.

3.2. The Corrosion Performance of the Coatings in Artificial Seawater

Figure 6a depicts the Nyquist plots of the CrN, CrTiN, and CrTiBN coatings during AC impedance testing. Figure 6b depicts the phase angle versus frequency plots of the CrN, CrTiN, and CrTiBN coatings. In the EIS impedance testing process, an electrochemical reaction occurs between the artificial seawater and the surfaces of the CrN, CrTiN, and CrTiBN coatings. Simultaneously, artificial seawater permeates through fine pores, coming

into contact with the substrate interface and engaging in electrochemical reactions [25]. In Figure 6a, Nyquist plots for the CrN, CrTiN, and CrTiBN coatings during AC impedance testing are presented. In Figure 6a, Nyquist plots for the CrN, CrTiN, and CrTiBN coatings during AC impedance testing are presented. All samples exhibit capacitive resistance arcs, comprising both smaller and larger diameter loops. A larger capacitive arc corresponds to greater impedance [39]. In comparison to uncoated 316 stainless steel, the CrN, CrTiN, and CrTiBN coatings all exhibit larger capacitive arcs. Among them, the CrTiBN coating exhibits the largest capacitive arc. Figure 6b depicts the phase angle plots of the CrN, CrTiN, and CrTiBN coatings. In general, when the phase angle in a Bode plot approaches 90 degrees, it indicates a more pronounced capacitive response of the coating. Throughout the low-frequency range, all coatings outperform uncoated 316 stainless steel, with the CrTiBN coating exhibiting the highest phase angle. This underscores the exceptional physical barrier properties of the three coatings, effectively guarding against electrolytic corrosion and enhancing substrate protection. Viewing it from a frequency standpoint, a broad frequency range highlights outstanding capacitive performance, indicating its efficient safeguarding of the substrate against seawater corrosion across a more extensive frequency spectrum [40]. In comparison among the three coatings, the CrTiBN coating exhibits the largest arc radius, as well as the highest phase angle and the broadest frequency range. This clearly suggests that, when compared to the other coatings, the CrTiBN coating boasts optimal corrosion resistance.

The EIS fitting analysis on the coatings was carried out with ZsimpWin 3.6 software, employing the equivalent circuit method and the circuit diagram illustrated in Figure 6c. In this context, R_s corresponds to the resistance of the electrolyte, which, in this case, is artificial seawater. R_{po} represents the resistance arising from the coating's pores, hindering the infiltration of the electrolyte. On the other hand, R_{ct} symbolizes the resistance to charge transfer between the thin film substrate and artificial seawater. Meanwhile, CPE_{po} and CPE_{dl} , respectively, stand for the capacitance linked with the coating and the double layer.

The results of the fitting are presented in Table 4. R_{ct} is a vital parameter, representing the corrosion resistance of thin films. Specifically, R_{ct} for the CrN, CrTiN, and CrTiBN coatings measures at $9.36 \times 10^5 \Omega \cdot \text{cm}^2$, $8.56 \times 10^5 \Omega \cdot \text{cm}^2$, and $1.18 \times 10^6 \Omega \cdot \text{cm}^2$, respectively. Remarkably, the CrTiBN coating stands out with the highest charge transfer resistance, underscoring its exceptional corrosion resistance relative to the other two coatings.

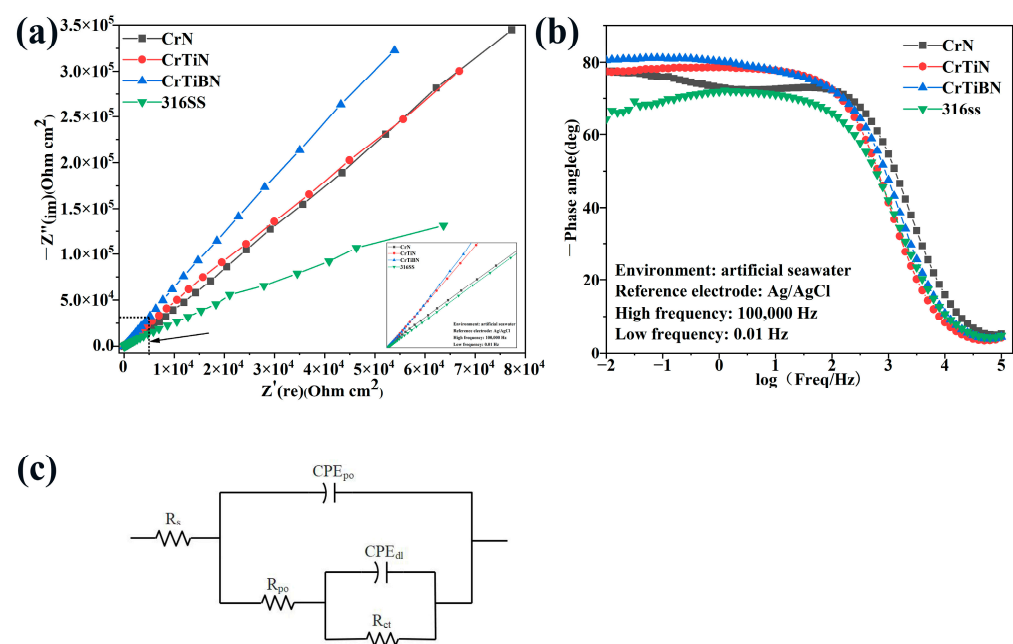
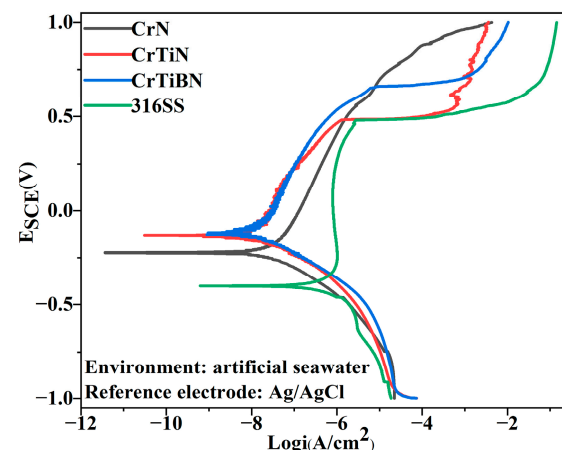


Figure 6. Nyquist plots (a), Bode phase angle plots (b), and Equivalent Circuit Diagram (c) of CrN, CrTiN, and CrTiBN coatings in seawater and the corresponding equivalent circuit models.

Table 4. Fitted results of EIS spectra for CrN, CrTiN, and CrTiBN coatings in artificial seawater.

Coatings	R_s ($\Omega \cdot \text{cm}^2$)	CPEpo ($\text{F} \cdot \text{cm}^2$)	R_{po} ($\Omega \cdot \text{cm}^2$)	CPEd1 ($\text{F} \cdot \text{cm}^2$)	R_{ct} ($\Omega \cdot \text{cm}^2$)
CrN	13.53	8.53×10^{-6}	3.49×10^5	2.01×10^{-5}	9.36×10^5
CrTiN	13.51	1.58×10^{-5}	3.35×10^5	1.95×10^{-5}	8.56×10^5
CrTiBN	9.95	1.55×10^{-5}	1.26×10^5	1.91×10^{-5}	1.18×10^6

Figure 7 depicts the potentiodynamic polarization curves of the CrN, CrTiN, and CrTiBN coatings in artificial seawater, along with the electrochemical E_{corr} acquired from fitting these curves, which are detailed in Table 5. Clearly, the E_{corr} values of the CrN, CrTiN, and CrTiBN coatings in artificial seawater are all below 0 V. Importantly, the E_{corr} of the CrTiN and CrTiBN coatings, measuring at -0.14 V and -0.11 V, respectively, is notably higher than that of the CrN coating and 316 stainless steel. The i_{corr} values of the CrN, CrTiN, and CrTiBN coatings have decreased by one order of magnitude compared to 316 stainless steel. Importantly, the CrTiBN coating exhibits the lowest i_{corr} value of 1.94×10^{-8} A/cm², whereas the i_{corr} values of the CrN and CrTiN coatings are relatively similar, measuring at 2.87×10^{-8} A/cm² and 3.06×10^{-8} A/cm², respectively. The R_p values of the CrN, CrTiN, and CrTiBN coatings have been reduced by two orders of magnitude compared to 316 stainless steel. The CrN coating has the lowest R_p value in artificial seawater, measuring 1230 k $\Omega \cdot \text{cm}^2$, while the CrTiBN coating displays the highest R_p value at 2470 k $\Omega \cdot \text{cm}^2$.

**Figure 7.** Tafel curves of CrN, CrTiN, and CrTiBN coatings in artificial seawater.**Table 5.** Electrochemical corrosion parameters inferred from Tafel plots.

Coatings	E_{corr} (V)	β_a (V)	β_c (V)	i_{corr} (A/cm ²)	R_p (k $\Omega \cdot \text{cm}^2$)
CrN	-0.22	4.11	8.14	2.87×10^{-8}	1230
CrTiN	-0.14	1.78	0.15	3.06×10^{-8}	2020
CrTiBN	-0.11	0.48	0.14	1.94×10^{-8}	2470
316	-0.40	2.55	4.11	9.52×10^{-7}	69

The results above indicate that the CrN, CrTiN, and CrTiBN coatings have all improved the corrosion resistance of the substrate. Among these coatings, the CrTiBN coating exhibits relatively higher corrosion potential, polarization resistance, and the lowest corrosion current, demonstrating excellent corrosion resistance [41]. This is attributed to the introduction of B elements, which disrupt the columnar crystal structure of the coatings and create an amorphous structure. This structural change enhances the compactness of the coatings and refines their grain size. At the microstructural level, it results in greater

closure of interfaces against microcracks and through-holes, reducing the interconnectivity of pores, and consequently enhancing corrosion resistance [42,43].

3.3. The Wear Performance of the Coatings in Artificial Seawater

Figure 8 depicts the friction coefficient curves and average steady-state friction coefficients of the CrN, CrTiN, and CrTiBN coatings during sliding against SiC balls in artificial seawater. Figure 8a illustrates an initial running-in period during which the friction coefficient experiences a sharp increase, primarily attributed to the presence of large particles and other defects on the coating surface. With the conclusion of the running-in phase, the friction between the coatings and SiC balls embeds or damages the larger abrasive particles, resulting in a smoother contact interface and a gradual stabilization of the friction coefficient values [16]. During sliding against SiC spheres, the friction coefficient of the CrN coating initially decreases from 0.18 to 0.15 within the first 200 m, subsequently rising to 0.22, and eventually stabilizing at approximately 0.22 beyond the 200 m mark. The friction coefficient of the CrTiN coating experiences an initial drop from 0.19 to 0.17 within the first 100 m, followed by a subsequent rise to 0.19. Between 100 and 500 m, the friction coefficient gradually decreases from 0.19 to 0.17. The friction coefficient of the CrTiBN coating initially increases from 0.16 to 0.19 within the first 10 m, subsequently dropping to 0.16 at 40 m, and ultimately stabilizing at approximately 0.16. As a result, it can be inferred that the CrTiBN coating reaches stability in a shorter time period. Among the three coatings illustrated in Figure 8b, the CrTiBN coating demonstrates the lowest steady-state friction coefficient, measuring at 0.16. In contrast, the CrTiN and CrN coatings have relatively higher steady-state friction coefficients, measuring 0.18 and 0.22, respectively. These friction coefficients are lower than that of the 316 stainless steel substrate, suggesting that the application of CrN, CrTiN, and CrTiBN coatings on the surface of 316 stainless steel effectively reduces its friction coefficient.

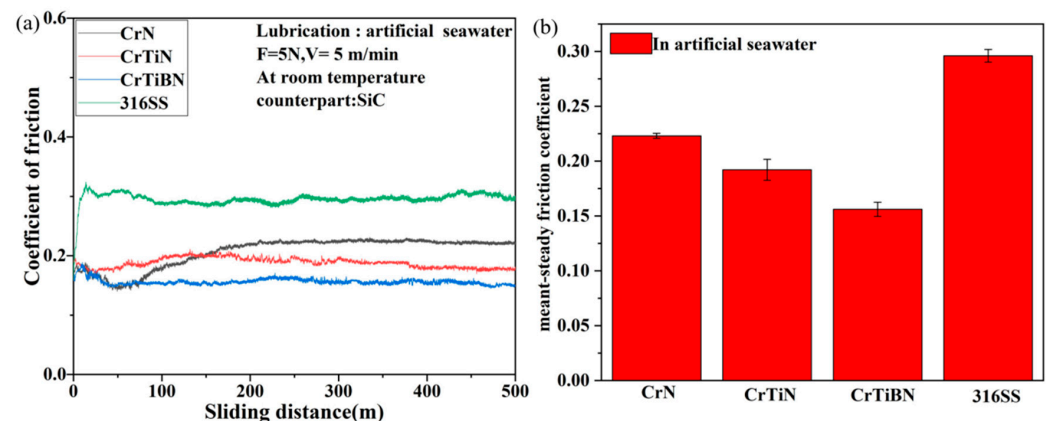


Figure 8. Friction coefficient curves (a) and average steady-state friction coefficients (b) of CrN, CrTiN, and CrTiBN coatings sliding against SiC balls in artificial seawater.

Figures 9 and 10 depict the wear and EDS images of the CrN, CrTiN, and CrTiBN coatings in contact with SiC in the friction pair, and Figure 10 presents the wear track images of these coatings. Indeed, the wear performance of coatings is intricately linked to their microstructure and mechanical characteristics. Enhanced surface hardness effectively mitigates coating wear and augments wear resistance. The XRD and XPS findings indicate that Ti elements are present in the form of TiN, while B elements exist in the BN phase in the CrTiBN coating. As indicated in Table 4, the introduction of Ti elements elevated the hardness of the CrN coating from 1965 HV to 2456 HV. However, post the introduction of B elements, the hardness of the CrTiBN coating stands at 2374 HV, closely mirroring that of the CrTiN coating.

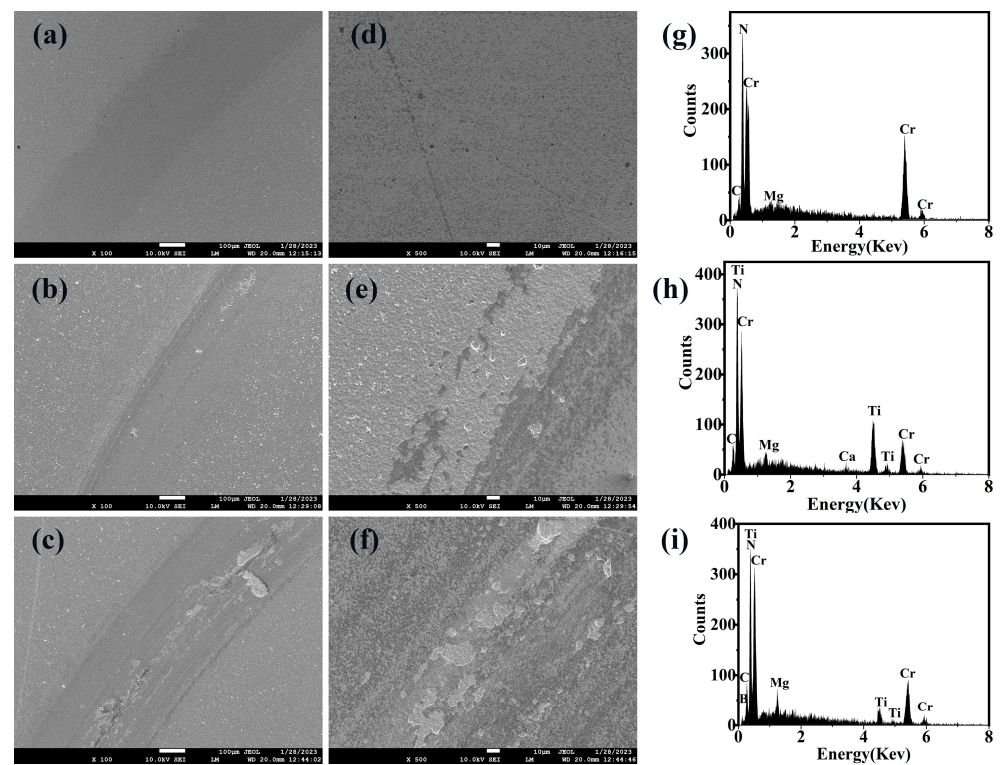


Figure 9. SEM (a–f) and EDS (g–i) images of wear tracks of CrN, CrTiN, and CrTiBN coatings.

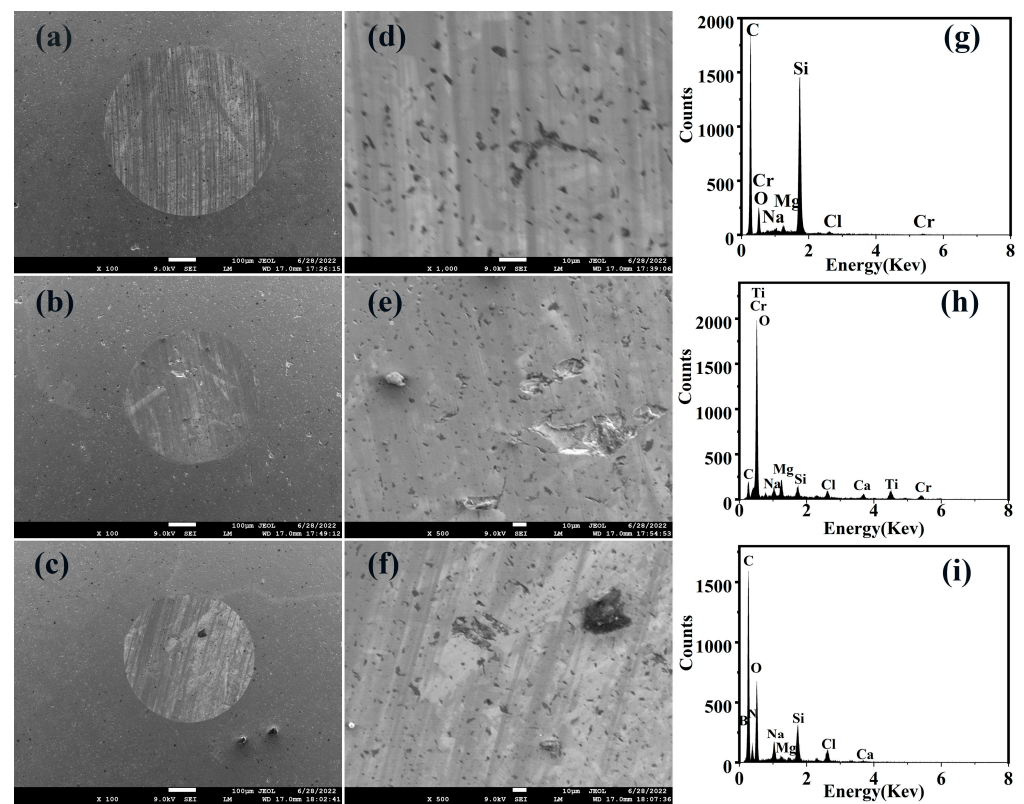


Figure 10. SEM (a–f) and EDS (g–i) images of wear tracks of SiC balls.

Moreover, the friction pair is intimately connected to the physical conditions of the contact interface, the friction material, and chemical reactions within the environment.

The CrN coating exhibits the widest wear track among the three coatings, measuring 330.3 μm in width, and it has a shallow depth of 0.10 μm (Figure 11). Importantly, there are no discernible grooves on the wear track's surface (Figures 9a,d and 10b). Compared to the other coatings, the CrN coating exhibits the most significant wear on the surface of the abraded SiC ball. The wear track on the SiC ball surface reveals not just the initial pores but also many deep grooves (Figure 10a), while the wear track surface is decorated with numerous fine scratch lines. At the center of the wear track on the SiC ball, the presence of Si, C, and Cr is detected. The results suggest that the wear debris from the CrN coating progressively transfers onto the SiC ball surface, signifying an abrasive wear mechanism in action.

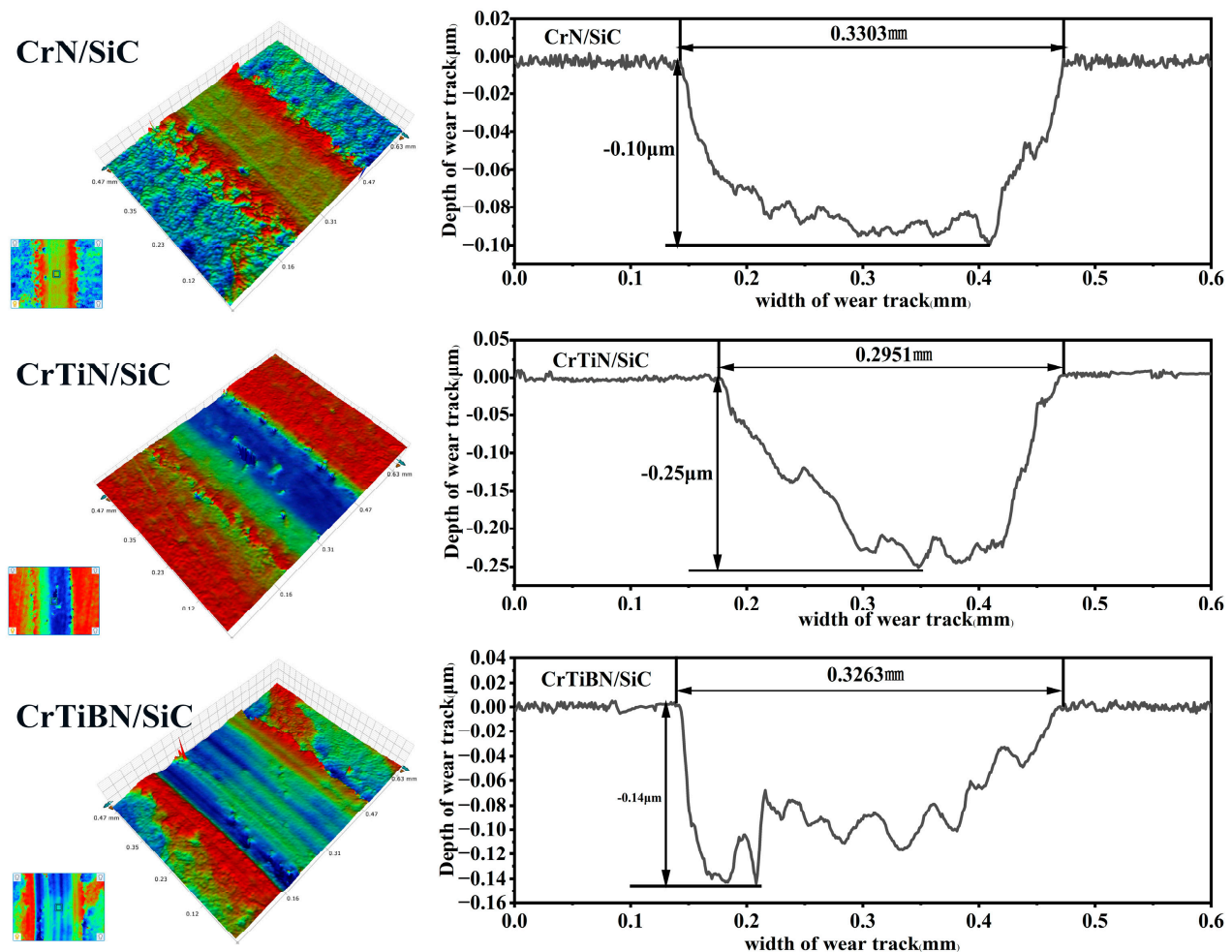


Figure 11. Wear section view of CrN, CrTiN, and CrTiBN coatings after tested in artificial seawater.

Regarding the CrTiN coating, it exhibits the greatest wear depth compared to the other two coatings, with a wear track depth of 0.25 μm (Figure 11). Importantly, clear deep grooves are evident on the CrTiN coating wear track, along with layered debris accumulation at the edges (Figures 9b,d and 10d). Particles on both the wear mark of the CrTiN coating and the surface of the SiC ball contain Ti, Cr, and O. Yan et al. [44] discovered that coatings with Ti elements tend to oxidize and generate TiO_2 at the wear interface. TiO_2 has a relatively loose microstructure compared to Cr_2O_3 debris, making it more susceptible to shearing. The results suggest that wear particles from the CrTiN coating progressively shift from the coating to the opposing wear interface, participating in friction as Cr_2O_3 and TiO_2 particles. Consequently, this leads to the creation of the deepest wear scar with a depth of 0.25 μm , characteristic of typical abrasive wear.

Regarding the CrTiBN coating, there are shallow wear scars on the wear track surface, and the wear track depth measures $0.14\text{ }\mu\text{m}$ (Figure 11). Noticeable delamination is present in the central region of the wear track, and in the worn area, a distinct stepwise delamination is evident (Figure 9a,d). According to the EDS spectroscopic analysis, the major components of the wear scar are Cr, Ti, B, and O. This suggests that during sliding friction, wear particles adhere to the coating friction interface, forming a layered debris structure, indicating an adhesive wear mechanism. In Figure 10, layered residues on the SiC ball are identified, consisting of C, Si, O, and B. These observations imply that wear particles from the CrTiBN coating gradually transfer onto the SiC ball surface. During sliding of the CrTiBN coating against the SiC ball in water, a stratified layer of H_3BO_3 can develop at the sliding interface, promoting fluid dynamic lubrication and thereby creating a self-lubrication effect [45].

A comprehensive analysis of the results depicted in Figures 9 and 10 indicates that the wear mechanism of the CrTiBN coating is adhesive wear, in contrast to the abrasive wear observed in the CrN and CrTiN coatings. In summary, the CrTiBN coating addresses the mechanical shortcomings linked to abrasive wear found in the CrN and CrTiN coatings, thereby enhancing the wear-resistant characteristics of these coatings.

Figure 12 depicts the wear rate graph of the CrN, CrTiN, and CrTiBN coatings after testing in artificial seawater. The wear rates of the CrN, CrTiN, and CrTiBN coatings are $1.81 \times 10^{-6}\text{ mm}^3/\text{Nm}$ (CrN), $1.08 \times 10^{-6}\text{ mm}^3/\text{Nm}$ (CrTiN), and $8.18 \times 10^{-7}\text{ mm}^3/\text{Nm}$ (CrTiBN), respectively, in alignment with the coating structural density. Following 500 m of abrasion with SiC spheres in artificial seawater, the trace depths of the three coatings are notably shallower than the coating thickness, affirming the coating durability.

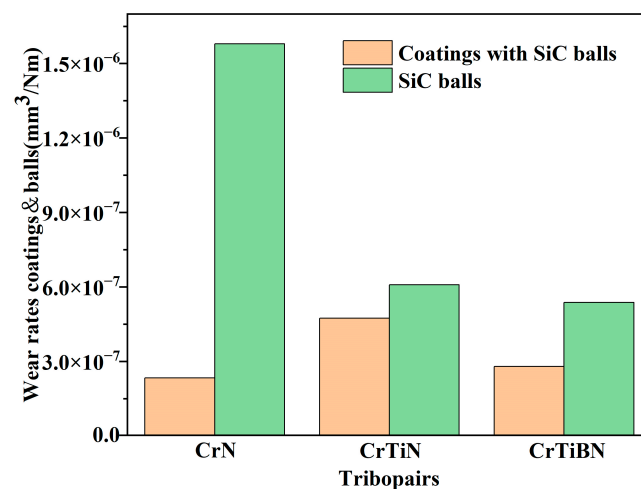


Figure 12. Wear rate of CrN, CrTiN, and CrTiBN coatings after tested in artificial seawater.

The wear resistance of the CrTiBN coating is significantly improved compared to that of the CrN and CrTiN coatings. As indicated with the prior XPS analysis, the presence of B elements is primarily in the form of a BN phase within the CrTiBN coating. This disrupts the growth of columnar crystals, refines the grain size, enhances coating density, and reduces coating defects. Generally, this enhancement can be credited to the reduced crystallite dimensions, the microstructure of the amorphous BN phase, and the elevated hardness of the CrTiBN coating [46].

3.4. Frictional Corrosion Behavior of Coatings in Artificial Seawater

Figure 13 depicts the variations in the Open Circuit Potential and coefficient of friction of the CrN, CrTiN, and CrTiBN coatings, as well as 316 stainless steel, throughout the three stages of static, sliding, and static in artificial seawater. During the immersion phase, the Open Circuit Potential (OCP) of all coatings and materials remains stable. However, at the beginning of the sliding stage, there is a significant drop in the OCP of

the samples, which can be attributed to the disruption of the passivation layer due to friction, as discussed earlier [47]. After the friction begins, a decrease in OCP is observed in all samples. Importantly, 316 stainless steel experiences the most substantial decrease in OCP during friction, indicating the lowest OCP value. Remarkably, the CrTiBN coating exhibits the highest OCP value during the friction process. After friction stops, the OCP of the specimens quickly recovers, gradually increasing, and eventually stabilizes. This is primarily because the surface of the sample quickly forms a dense passive film after friction ceases. With increasing immersion time, the passivation film becomes denser and more stable.

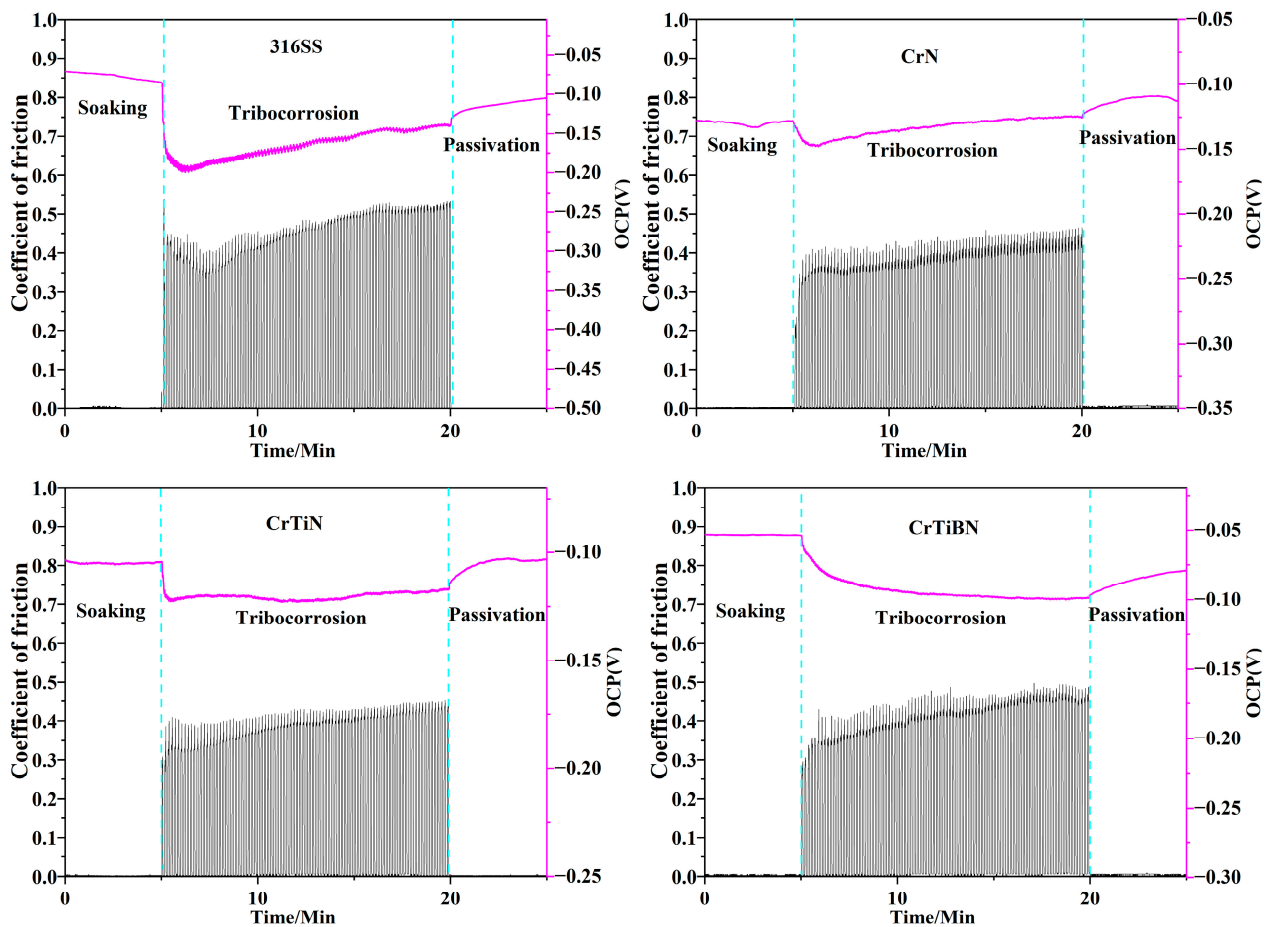


Figure 13. Change in OCP and COF during tribocorrosion test in seawater.

In summary, throughout the entire duration of friction, the Open Circuit Potential (OCP) of the CrN, CrTiN, and CrTiBN coatings consistently exceeds that of 316 stainless steel. Importantly, the CrTiBN coating exhibits the highest OCP, highlighting its outstanding ability to protect 316 stainless steel from corrosion in marine environments.

4. Conclusions

In this research context, CrN, CrTiN, and CrTiBN coatings were fabricated utilizing multi-arc ion plating. Subsequently, their corrosion resistance and wear durability were extensively examined in an artificial seawater environment. The research indicated that the incorporation of Ti and B elements into the CrN coating resulted in substantial grain refinement and increased coating density, ultimately enhancing coating quality and improving wear and corrosion resistance. Electrochemical impedance spectroscopy tests revealed that the CrTiBN coating demonstrates the highest polarization resistance, the maximal phase angle, and the most extensive frequency range. In potentiodynamic polarization tests, the CrTiBN coating exhibits the most positive potential of -0.11 V, a polarization

resistance of $2470 \text{ k}\Omega\cdot\text{cm}^2$, and the lowest current density at $1.94 \times 10^{-8} \text{ A/cm}^2$. The artificial seawater friction experiments revealed that the CrTiBN coating exhibits the lowest friction coefficient of 0.16 and a wear rate of $8.18 \times 10^{-7} \text{ mm}^3/\text{Nm}$, which is attributable to its compact coating structure and exceptional corrosion resistance. The results of electrochemical fretting corrosion tests indicated that the CrTiBN coating has the most positive value of the corrosion potential, underscoring its exceptional wear–corrosion resistance during the entire friction process.

Author Contributions: Conceptualization, Methodology, Writing—Review and Editing, M.L.; Visualization, Data Curation, Y.Y.; Resources, Supervision, C.Z.; Visualization, Investigation, C.T.; Validation, Y.X. All authors have read and agreed to the published version of the manuscript.

Funding: This work was supported by the Innovation team project of Guangdong Universities (2020KCXTD032), Science and Technology Project of Zhanjiang (2019A03009, 2022A0100, 2023B01012), Natural Science Foundation of Guangdong Province (2021A1515011928, 2022A1515011137), and Lingnan Normal University Research Project (LY2203).

Institutional Review Board Statement: Not applicable.

Informed Consent Statement: Not applicable.

Data Availability Statement: The data that support the findings of this study are available within the article.

Conflicts of Interest: The authors declare no conflict of interest.

References

1. Wood, R.J.K. Marine wear and tribocorrosion. *Wear* **2017**, *376*, 893–910. [\[CrossRef\]](#)
2. Li, L.; Liu, L.L.; Li, X.; Guo, P.; Ke, P.; Wang, A. Enhanced tribocorrosion performance of Cr/GLC multilayered films for marine protective application. *ACS Appl. Mater. Interfaces* **2018**, *10*, 13187–13198. [\[CrossRef\]](#) [\[PubMed\]](#)
3. Li, Z.; Yu, H.; Sun, D. The tribocorrosion mechanism of aluminum alloy 7075-T6 in the deep ocean. *Corros. Sci.* **2021**, *183*, 109306. [\[CrossRef\]](#)
4. Wu, D.; Guan, Z.; Cheng, Q.; Guo, W.; Tang, M.; Liu, Y. Development of a friction test apparatus for simulating the ultra-high pressure environment of the deep ocean. *Wear* **2020**, *452*, 203294. [\[CrossRef\]](#)
5. Albrimi, Y.A.; Eddib, A.; Douch, J.; Berghoute, Y.; Hamdani, M.; Souto, R.M. Electrochemical behaviour of AISI 316 austenitic stainless steel in acidic media containing chloride ions. *Int. J. Electrochem. Sci.* **2011**, *6*, 4614–4627. [\[CrossRef\]](#)
6. Ma, F.; Li, J.; Zeng, Z.; Gao, Y. Tribocorrosion behaviour of F690 and 316L steel in artificial seawater. *Lubr. Sci.* **2018**, *30*, 365–375. [\[CrossRef\]](#)
7. Kumar, N.; Kumar, A.; Singh, A.K.; Das, G. Corrosion resistance of austenitic Cr-Ni stainless steel in 1 M HCl. *Int. J. Mech. Eng. Robot. Res.* **2014**, *3*, 21.
8. Shan, L.; Wang, Y.; Zhang, Y.; Zhang, Q.; Xue, Q. Tribocorrosion behaviors of PVD CrN coated stainless steel in seawater. *Wear* **2016**, *362*, 97–104. [\[CrossRef\]](#)
9. Vite, M.; Moreno-Ríos, M.; Hernández, E.G.; Laguna-Camacho, J. A study of the abrasive resistance of sputtered CrN coatings deposited on AISI 316 and AISI H13 steel substrates using steel particles. *Wear* **2011**, *271*, 1273–1279. [\[CrossRef\]](#)
10. Zhang, G.A.; Yan, P.X.; Wang, P.; Chen, Y.M.; Zhang, J.Y. The structure and tribological behaviors of CrN and Cr-Ti-N coatings. *Appl. Surf. Sci.* **2007**, *253*, 7353–7359. [\[CrossRef\]](#)
11. Kabir, M.S.; Munroe, P.; Zhou, Z.; Xie, Z. Scratch adhesion and tribological behaviour of graded Cr/CrN/CrTiN coatings synthesized by closed-field unbalanced magnetron sputtering. *Wear* **2017**, *380*, 163–175. [\[CrossRef\]](#)
12. Ding, X.Z.; Zeng, X.T. Structural, mechanical and tribological properties of CrAlN coatings deposited by reactive unbalanced magnetron sputtering. *Surf. Coat. Technol.* **2005**, *200*, 1372–1376. [\[CrossRef\]](#)
13. Barshilia, H.C.; Selvakumar, N.; Deepthi, B.; Rajam, K. A comparative study of reactive direct current magnetron sputtered CrAlN and CrN coatings. *Surf. Coat. Technol.* **2006**, *201*, 2193–2201. [\[CrossRef\]](#)
14. Contreras, E.; Galindez, Y.; Rodas, M.A.; Bejarano, G.; Gómez, M.A. CrVN/TiN nanoscale multilayer coatings deposited by DC unbalanced magnetron sputtering. *Surf. Coat. Technol.* **2017**, *332*, 214–222. [\[CrossRef\]](#)
15. Geng, Z.; Wang, H.; Wang, C.; Wang, L.; Zhang, G. Effect of Si content on the tribological properties of CrSiN films in air and water environments. *Tribol. Int.* **2014**, *79*, 140–150. [\[CrossRef\]](#)

16. Ye, Y.; Wang, Y.; Wang, C.; Li, J.; Yao, Y. An analysis on tribological performance of CrCN coatings with different carbon contents in seawater. *Tribol. Int.* **2015**, *91*, 131–139. [[CrossRef](#)]
17. Budna, K.P.; Neidhardt, J.; Mayrhofer, P.H.; Mitterer, C. Synthesis–structure–property relations for Cr–B–N coatings sputter deposited reactively from a Cr–B target with 20 at% B. *Vacuum* **2008**, *82*, 771–776. [[CrossRef](#)]
18. Zhang, G.; Wang, L.; Yan, P.; Xue, Q. Structure and mechanical properties of Cr–B–N films deposited by reactive magnetron sputtering. *J. Alloys Compd.* **2009**, *486*, 227–232. [[CrossRef](#)]
19. Ma, Q.; Zhou, F.; Gao, S.; Wu, Z.; Wang, Q.; Chen, K.; Zhou, Z.; Li, L.K.-Y. Influence of boron content on the microstructure and tribological properties of Cr–BN coatings in water lubrication. *Appl. Surf. Sci.* **2016**, *377*, 394–405. [[CrossRef](#)]
20. Chang, Y.-Y.; Chung, C.-H.; Tsai, Z.-H.; Tsai, J.-M. Tribological and mechanical properties of AlCrBN hard coating deposited using cathodic arc evaporation. *Surf. Coat. Technol.* **2022**, *432*, 128097. [[CrossRef](#)]
21. Kong, J.Z.; Hou, T.J.; Wang, Q.Z.; Yin, L.; Zhou, F.; Zhou, Z.F.; Li, L.K.Y. Influence of titanium or aluminum doping on the electrochemical properties of CrN coatings in artificial seawater. *Surf. Coat. Technol.* **2016**, *307*, 118–124. [[CrossRef](#)]
22. Lu, C.Y.; Diyatmika, W.; Lou, B.S.; Lu, Y.C.; Duh, J.G.; Lee, J.W. Influences of target poisoning on the mechanical properties of TiCrBN thin films grown by a superimposed high power impulse and medium-frequency magnetron sputtering. *Surf. Coat. Technol.* **2017**, *332*, 86–95. [[CrossRef](#)]
23. Ho, L.W.; Lee, J.W.; Chen, H.W.; Chan, Y.C.; Duh, J.G. Structure and mechanical property evaluation of Cr–Ti–B–N coatings. *Thin Solid Film.* **2013**, *544*, 380–385. [[CrossRef](#)]
24. Lu, C.Y.; Diyatmika, W.; Lou, B.S.; Lee, J.W. Superimposition of high power impulse and middle frequency magnetron sputtering for fabrication of CrTiBN multicomponent hard coatings. *Surf. Coat. Technol.* **2018**, *350*, 962–970. [[CrossRef](#)]
25. Wang, Q.; Zhou, F.; Zhou, Z.; Li, L.K.-Y.; Yan, J. An investigation on the crack resistance of CrN, CrBN and CrTiBN coatings via nanoindentation. *Vacuum* **2017**, *145*, 186–193. [[CrossRef](#)]
26. Yu, L.; Luo, H.; Bian, J.; Ju, H.; Xu, J. Research on microstructure, mechanical and tribological properties of Cr–Ti–BN films. *Coatings* **2017**, *7*, 137. [[CrossRef](#)]
27. Wang, Q.; Zhou, F.; Wang, X.; Chen, K.; Wang, M.; Qian, T.; Li, Y. Comparison of tribological properties of CrN, TiCN and TiAlN coatings sliding against SiC balls in water. *Appl. Surf. Sci.* **2011**, *257*, 7813–7820. [[CrossRef](#)]
28. ASTM D1141-98; Standard Practice for the Preparation of Substitute Ocean Water. ASTM: West Conshohocken, PA, USA, 1998.
29. ASTM G102-89e1; Standard Practice for Calculation of Corrosion Rates and Related Information from Electrochemical Measurements. ASTM: West Conshohocken, PA, USA, 2015.
30. Goto, H.; Akao, N.; Hara, N.; Sugimoto, K. Pinhole Defect Density of CrN_x Thin Films Formed by Ion-Beam-Enhanced Deposition on Stainless Steel Substrates. *J. Electrochem. Soc.* **2007**, *154*, C189. [[CrossRef](#)]
31. Zhou, S.Y.; Yan, S.J.; Han, B.; Yang, B.; Lin, B.Z.; Zhang, Z.D.; Ai, Z.W.; Pelenovich, V.O.; Fu, D.J. Influence of modulation period and modulation ratio on structure and mechanical properties of TiBN/CrN coatings deposited by multi-arc ion plating. *Appl. Surf. Sci.* **2015**, *351*, 1116–1121. [[CrossRef](#)]
32. Feng, N.; Wang, Q.; Zheng, A.; Zhang, Z.; Fan, J.; Liu, S.B.; Amoureux, J.-P.; Deng, F. Understanding the high photocatalytic activity of (B, Ag)-codoped TiO₂ under solar-light irradiation with XPS, solid-state NMR, and DFT calculations. *J. Am. Chem. Soc.* **2013**, *135*, 1607–1616. [[CrossRef](#)]
33. Wu, Y.; Liu, X.; Yang, Z.; Gu, L.; Yu, Y. Nitrogen-Doped Ordered Mesoporous Anatase TiO₂ Nanofibers as Anode Materials for High Performance Sodium-Ion Batteries. *Small* **2016**, *12*, 3522–3529. [[CrossRef](#)] [[PubMed](#)]
34. Aissani, L.; Fellah, M.; Nouveau, C.; Abdul Samad, M.; Montagne, A.; Iost, A. Structural and mechanical properties of Cr–Zr–N coatings with different Zr content. *Surf. Eng.* **2020**, *36*, 69–77. [[CrossRef](#)]
35. Ahmad, P.; Khandaker, M.U.; Amin, Y.M. Synthesis of boron nitride nanotubes by Argon supported Thermal Chemical Vapor Deposition. *Phys. E Low-Dimens. Syst. Nanostruct.* **2015**, *67*, 33–37. [[CrossRef](#)]
36. Ze, S.; Dejun, K.; Wei, L. Surface-interface microstructures and binding strength of cathodic arc ion plated TiCN coatings on YT14 cutting tools. *Surf. Interface Anal.* **2017**, *49*, 488–494. [[CrossRef](#)]
37. Tian, C.X.; Wang, Z.S.; Zou, C.W.; Tang, X.S.; Xie, X.; Li, S.Q.; Laing, F.; Li, Z.F.; Liu, Y.F.; Su, F.H. Ternary and quaternary TiBN and TiBCN nanocomposite coatings deposited by arc ion plating. *Surf. Coat. Technol.* **2019**, *359*, 445–450. [[CrossRef](#)]
38. Lide, D.R. (Ed.) *CRC Handbook of Chemistry and Physics*; CRC Press: Boca Raton, FL, USA, 2004.
39. Liu, C.; Bi, Q.; Matthews, A.E.I.S. EIS comparison on corrosion performance of PVD TiN and CrN coated mild steel in 0.5 N NaCl aqueous solution. *Corros. Sci.* **2001**, *43*, 1953–1961. [[CrossRef](#)]
40. Fu, Y.; Zhou, F.; Wang, Q.; Zhang, M.; Zhou, Z. Electrochemical and tribocorrosion performances of CrMoSiCN coating on Ti-6Al-4V titanium alloy in artificial seawater. *Corros. Sci.* **2020**, *165*, 108385. [[CrossRef](#)]
41. Chang, C.H.; Huang, T.C.; Peng, C.W.; Yeh, T.C.; Lu, H.I.; Hung, W.I.; Wang, C.J.; Yang, T.I.; Yeh, J.M. Novel anticorrosion coatings prepared from polyaniline/graphene composites. *Carbon* **2012**, *50*, 5044–5051. [[CrossRef](#)]
42. Lin, C.H.; Duh, J.G. Electrochemical impedance spectroscopy (EIS) study on corrosion performance of CrAlSiN coated steels in 3.5 wt% NaCl solution. *Surf. Coat. Technol.* **2009**, *204*, 784–787. [[CrossRef](#)]
43. Jehn, H.A. Improvement of the corrosion resistance of PVD hard coating–substrate systems. *Surf. Coat. Technol.* **2000**, *125*, 212–217. [[CrossRef](#)]
44. Yan, Z.; Jiang, D.; Gao, X.; Hu, M.; Wang, D.; Fu, Y.; Sun, J.; Feng, D.; Weng, L. Friction and wear behavior of TiN films against ceramic and steel balls. *Tribol. Int.* **2018**, *12*, 61–69. [[CrossRef](#)]

45. Zhou, F.; Adachi, K.; Kato, K. Friction and wear behavior of BCN coatings sliding against ceramic and steel balls in various environments. *Wear* **2006**, *261*, 301–310. [[CrossRef](#)]
46. Wang, L.; Zhang, G.; Wood, R.J.K.; Wang, S.C.; Xue, Q. Fabrication of CrAlN nanocomposite films with high hardness and excellent anti-wear performance for gear application. *Surf. Coat. Technol.* **2010**, *204*, 3517–3524. [[CrossRef](#)]
47. Bayón, R.; Igartua, A.; González, J.J.; De Gopegui, U.R. Influence of the carbon content on the corrosion and tribocorrosion performance of Ti-DLC coatings for biomedical alloys. *Tribol. Int.* **2015**, *88*, 115–125. [[CrossRef](#)]

Disclaimer/Publisher’s Note: The statements, opinions and data contained in all publications are solely those of the individual author(s) and contributor(s) and not of MDPI and/or the editor(s). MDPI and/or the editor(s) disclaim responsibility for any injury to people or property resulting from any ideas, methods, instructions or products referred to in the content.